Research Article Vol. 33, No. 4 / 24 Feb 2025 / Optics Express 6987
Optics EXPRESS

Robustness of lensless single random phase encoding systems to image sensor pixel size

SAURABH GOSWAMI, GOKUL KRISHNAN, AND BAHRAM JAVIDI*

Electrical Engineering Department, University of Connecticut, 371 Fairfield Road, Unit 2157 Storrs, Connecticut 06269, USA
bahram.javidi@uconn.edu

Abstract: In this paper, we propose a procedure to analyze lensless single random phase encoding (SRPE) systems to assess their robustness to variations in image sensor pixel size as the input signal frequency is varied. We use wave propagation to estimate the maximum pixel size to capture lensless SRPE intensity patterns such that an input signal frequency can be captured accurately. Lensless SRPE systems are contrived by placing a diffuser in front of an image sensor such that the optical field coming from an object can be modulated before its intensity signature is captured at the image sensor. Since diffuser surfaces contain very fine features, the captured intensity patterns always contain high spatial frequencies regardless of the input frequencies. Hence, a conventional Nyquist-criterion-based treatment of this problem would not give us a meaningful characterization. We propose a theoretical estimate on the upper limit of the image sensor pixel size such that the variations in the input signal are adequately captured in the sensor pixels. A numerical simulation of lensless SRPE systems using angular spectrum propagation and mutual information verifies our theoretical analysis. The simulation estimate of the sampling criterion matches very closely with our proposed theoretical estimate. We provide a closed-form estimate for the maximum sensor pixel size as a function of input frequency and system parameters such that an input signal frequency can be captured accurately, making it possible to optimize general-purpose SRPE systems. Our results show that lensless SRPE systems have a much greater robustness to sensor pixel size compared with lens based systems, which makes SRPE useful for exotic imagers when pixel size is large. To the best of our knowledge, this is the first report to investigate sampling of lensless SRPE systems as a function of input image frequency and physical parameters of the system to estimate the maximum image sensor pixel size.

1. Introduction

When light emanating from an object of interest propagates through an optical imaging setup and gets captured at an image sensor, a continuous field is rendered at discrete spatial locations. This discretization, commonly known as sampling, inevitably causes a change between the incident field and the recorded field. An optimal image sensor ensures that this change does not corrupt the information content of the incident signal. Establishing such an optimality criterion for sampling requires precise knowledge of the signal corruption that takes place at the critical sampling rate. For linear shift invariant (LSI) systems (i.e., systems that do not redistribute the frequency contents of a signal), this corruption happens to be aliasing, i.e., high frequencies in the incident field appear as low frequencies in the captured field. For such devices, the famed Nyquist criterion [1] guides the choice of an optimal sampling rate. In other words, aliasing and Nyquist criterion go hand-in-hand.

There are, however, useful imaging systems successfully employed for imaging/sensing purposes that cause a redistribution of the frequency content as the optical field travels from the object to the image sensor. Lensless imaging systems [2–9] are a prime example of these. In this paper, we focus on single diffuser-based lensless imaging systems, i.e., single random phase

#546066 https://doi.org/10.1364/OE.546066
Journal © 2025 Received 25 Oct 2024; revised 31 Dec 2024; accepted 28 Jan 2025; published 11 Feb 2025

Optics EXPRESS

encoding (SRPE) systems [3–8]. The use of lenses in conventional imaging/sensing devices makes the corresponding setups bulky and expensive. Moreover, increasing the lens numerical aperture, which majorly influences the resolution of such devices, requires manufacturing of a large lens with precise specifications, making the process time-consuming and expensive. Replacing the lens with a diffuser makes the devices much more compact, field-portable and less expensive. Diffuser-based lensless systems also offer enhanced field-of-view and depth-of-field [10]. Recent studies with SRPE systems have shown that the intensity patterns captured with these systems can directly be used (without computational reconstruction) to successfully classify between diseased and healthy biological cells [3–6]. The classification performance of such systems has also been shown to be robust to noise [5] and dimensionality reduction [6] of the intensity patterns. Other diffuser-based lensless systems [9,11] have been able to reconstruct a complete three-dimensional field and even video from only a handful samples collected from the intensity pattern captured at the image sensor.

Given the benefits and the expanding applicability of diffuser-based lensless imaging systems, it is important to formulate a sampling criterion for such systems to optimize their usability in information-critical tasks. It is beneficial to investigate the nature of data corruption that manifests itself in the intensity pattern due to sampling. Typical diffusers used in SRPE systems have extremely fine surface features [7,8]. When an input signal is incident on the diffuser, the diffuser modulates the input frequency contents with the high frequency of its surface features. Since these features are often much smaller than the pixel size, aliasing becomes inescapable for the captured patterns. Hence, a naïve application of the Nyquist criterion will prescribe infeasibly small pixels to accurately sample the output intensity pattern. However, the successful employment of such systems in the aforementioned previous works with standard cameras lead us to believe that directly using Nyquist criterion on the intensity patterns is not accurate. In the investigation of a sampling criterion for such systems, the aliasing of high frequency diffuser surface variations should be immaterial as long as the underlying object frequencies do not get corrupted.

In this work, we consider a typical lensless SRPE system with a diffuser placed along the path of an object field traveling towards the image sensor. We use wave propagation to derive a critical maximum image sensor pixel size which would accurately capture the contribution of an input frequency. We also predict what corruption the intensity pattern will undergo once the sensor pixel size exceeds this maximum sensor pixel size value. We then perform numerical simulation to investigate how the lensless SRPE system performs in the neighborhood of this maximum pixel size. If the simulations show the predicted corruption occurring at the predicted maximum pixel size, it verifies our reasoning and establishes our method as a valid sampling criterion. We provide a closed-form expression for the maximum sensor pixel size such that an input signal frequency can be captured accurately, as a function of input object frequency and the physical parameters of an SRPE system. Our analysis shows that lensless SRPE systems have a much greater robustness to sensor pixel size compared with lens based systems which makes lensless SRPE systems useful for exotic imagers which have large pixel size. This is the first report to investigate sampling of lensless SRPE systems by using wave propagation as a function of input image frequency and physical parameters of the system to estimate the maximum image sensor pixel size.

The rest of this paper is organized as follows. In section 2, we briefly describe our lensless SRPE system, sampling operation in cameras, sampling criterion for lens-based systems, our proposed sampling criterion for lensless SRPE systems, and the statistical metrics used for analysis in this study. In section 3, we report and discuss the results obtained through simulations based on the theory discussed in section 2. Finally, we present the conclusions of our study in section 4.

Optics EXPRESS

2. Methodology

2.1. Wave propagation in lensless single random phase encoding systems

The propagation of complex optical field through lensless SRPE systems can be mathematically modeled using the principles of wave optics [1]. As shown in Fig. 1, SRPE systems consist of two key components: a high-scattering diffuser, and an image sensor. During its operation, light of wavelength λ from an object first travels a distance z_1 to reach the diffuser. The surface roughness of the diffuser modulates the incoming signal with a spatially varying random phase. This modulated field then further travels a distance z_2 to reach the image sensor where the intensity of the complex field is recorded.

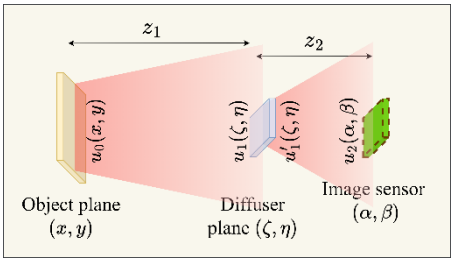

Fig. 1. A schematic diagram of our lensless single random phase encoding system.

Following the modeling principles of [7,8], we used angular spectrum propagation [1] to mathematically simulate a lensless SRPE system. As shown in Fig. 1, the co-ordinates on the object plane are represented as (x, y), those on the diffuser plane are denoted as (ζ, η) and finally, (α, β) describes points on the image sensor plane. For all numerical simulations in this work, we begin with a sinusoidally varying amplitude on the object plane, i.e., our input $u_0(x, y)$ can be written as:

$$u_0(x, y) = \cos(2\pi \overline{f_x} x) \tag{1}$$

where $\overline{f_x}$ denotes the spatial frequency of the sinusoid. This field propagates a distance z_1 to end up at the diffuser. The field right before the diffuser can be written as:

$$u_1(\zeta, \eta) = u_0(\zeta, \eta) * h_D(\zeta, \eta) * \frac{1}{2\pi} \frac{z_1}{r_1} \left(\frac{1}{r_1} - jk \right) \frac{\exp(jkr_1)}{r_1} \tag{2}$$

where $r_1 = \sqrt{\zeta^2 + \eta^2 + z_1^2}$, $k = 2\pi/\lambda$ is the propagation constant of the light, and $h_D(\zeta, \eta)$ is a filter which eliminates the spatial frequencies that the diffuser would not capture due to its finite dimensions [7,8]. The diffuser modulates this signal with a spatially varying random phase $\phi(\zeta, \eta)$ which is uniformly distributed within the range $(-\pi, \pi]$. For a thin diffuser, this operation can be described by a multiplicative diffuser transmittance function $t_D(\zeta, \eta)$ [5–8] such that:

$$t_D(\zeta, \eta) = \exp(j\phi(\zeta, \eta)) Rect\left(\frac{\zeta}{D_\zeta}, \frac{\eta}{D_\eta} \right) \tag{3}$$

where (D_ζ, D_η) is the spatial dimension of the diffuser. Hence, the modulated signal can be written as:

$$u_1'(\zeta, \eta) = u_1(\zeta, \eta) \times t_D(\zeta, \eta) \tag{4}$$

This modulated signal further travels a distance z_2 to end up at the sensor. The field $u_2(\alpha, \beta)$ at the sensor can be expressed as follows:

$$u_2(\alpha, \beta) = u_1'(\alpha, \beta) * h_S(\alpha, \beta) * \frac{1}{2\pi} \frac{z_2}{r_2} \left(\frac{1}{r_2} - jk \right) \frac{\exp(jkr_2)}{r_2} \tag{5}$$

Optics EXPRESS

where $r_2 = \sqrt{\alpha^2 + \beta^2 + z_2^2}$ and $h_S(\alpha, \beta)$ is a filter that eliminates frequencies which the sensor would not be able to collect due to its finite size [7,8]. The sensor collects the intensity $i(\alpha, \beta)$ of this field:

$$i(\alpha, \beta) = |u_2(\alpha, \beta)|^2 \tag{6}$$

The next section describes how this continuous intensity distribution $i(\alpha, \beta)$ is collected at image sensor pixels. It is worthwhile to note that we are not proposing a new modeling pipeline for this system. The propagations have been performed using angular spectrum propagation and the diffuser model used in Eq. (3) is an established model that has been used in several previous studies [5–8]. We also note here that our analysis most closely pertains to holographic diffusers that use pseudorandom structures to scatter light within a cone described by their scattering angle. Such diffusers are different from Lambertian diffusers which evenly scatter light in all directions. In this work, we aim to provide a general formulation that remains valid for any scattering angle of holographic diffusers.

2.2. Sampling operation in cameras

From the source object to right before the intensity is recorded (see Fig. 1), the field is continuous. However, sensors record intensities of this field at discrete pixel locations (mp_α, np_β) where (p_α, p_β) are the pixel sampling rates of the image sensors along axes α and β. For the sake of simplicity, we shall assume that (p_α, p_β) are also the dimensions of each pixel.

Each pixel on an image sensor has a finite area over which the intensity of the incoming field assumes a continuous spatial distribution. While sampling, the sensor collects the average intensity value over each pixel. Mathematically, this operation can be described using two steps. At first, a linear shift-invariant (LSI) filter with a finite averaging window-size computes a sequence $i_\Sigma(\alpha, \beta)$ of spatial averages over the entire sensor [12], i.e.,

$$i_\Sigma(\alpha, \beta) = u_2(\alpha, \beta) * p(\alpha, \beta) \tag{7}$$

where $*$ denotes a linear convolution, and $p(\alpha, \beta)$ denotes the averaging operation by pixel. Since it is essentially a low pass filtering, it removes all the frequencies above $(1/p_\alpha, 1/p_\beta)$. Afterwards, this averaged sequence $i_\Sigma(\alpha, \beta)$ is sampled at discrete locations (mp_α, np_β). Post-sampling, this sampled intensity distribution is indexed with only $[m, n]$. Hence, the sampled distribution $i_S[m, n]$ can be written as:

$$i_S[m, n] = i_\Sigma(\alpha, \beta) \times \sum\nolimits_{(m,n)} \delta(\alpha - mp_\alpha, \beta - np_\beta) \tag{8}$$

where $\delta(\cdot, \cdot)$ denotes a dirac-delta function. Figure 2 shows a schematic diagram of the pixel sampling operation.

This sampling operation has effects on the frequency content of the signal. Essentially, the frequency spectrum of the intensity $i_\Sigma(\alpha, \beta)$ gets uniformly repeated over the entire frequency plane at a period of $(1/p_\alpha, 1/p_\beta)$. If $i_\Sigma(\alpha, \beta)$ contains frequencies above $(1/2p_\alpha, 1/2p_\beta)$, sampling process causes aliasing, i.e., high frequencies in the $i_\Sigma(\alpha, \beta)$ show up as low frequencies in $i_S[m, n]$. The next section discusses the Nyquist criterion to avoid aliasing in images captured with lens-based systems.

2.3. Nyquist sampling criterion for lens-based systems

In typical imaging applications, the lenses that are used are biconvex with positive focal lengths. Reference [1] has shown that for such lenses, assuming the magnification is unity (to avoid scaling between input and output frequencies), the relation between input complex object field

Optics EXPRESS

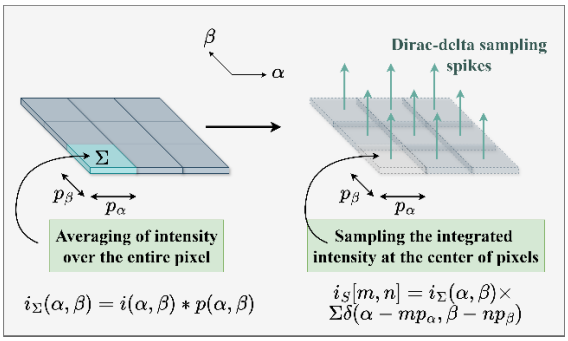

Fig. 2. Pixel averaging and sampling operation on an image sensor.

$u_0(x,y)$ (Eq. (1)) and the output complex image field $u_2(\alpha,\beta)$ (Eq. (5)) can be expressed as a linear convolution:

$$u_2(\alpha,\beta) = u_0(\alpha,\beta) * h_l(\alpha,\beta) \tag{9}$$

where $h_l(\alpha,\beta)$ is a filter that represents the effect of the lens. It is mathematically expressed as follows [1]:

$$h_l(\alpha,\beta) = \frac{1}{\lambda^2 z_1 z_2} \iint_{-\infty}^{\infty} P(\zeta,\eta) \times \exp\left(-j\frac{2\pi}{\lambda z_2}(\alpha\zeta + \beta\eta)\right) d\zeta\, d\eta \tag{10}$$

where $P(\zeta,\eta)$ is the pupil function of the lens, z_1 is the distance from the object to the lens, and z_2 is the distance between the lens and the image plane. To avoid frequency scaling between input and output, we shall assume $z_1 = z_2$.

For a single cosine input as in Eq. (1), the output field $u_2(\alpha,\beta)$ will have the following form:

$$u_2(\alpha,\beta) = A_l(\overline{f_x}) \cos(2\pi\overline{f_x}\alpha + \phi_l(\overline{f_x})) \tag{11}$$

where $A_l(\overline{f_x})$ and $\phi_l(\overline{f_x})$ are the amplitude and the phase shift accumulated due to the LSI filtering operation. The intensity $i(\alpha,\beta)$ of this field will be:

$$i(\alpha,\beta) = |u_2(\alpha,\beta)|^2 = \frac{|A_l(\overline{f_x})|^2}{2}(1 + \cos(4\pi\overline{f_x}\alpha + 2\phi_l(\overline{f_x}))) \tag{12}$$

Hence, for an input sinusoid of frequency $\overline{f_x}$, the output intensity has a maximum frequency of $2\overline{f_x}$. If we would like to sample this signal without aliasing, Nyquist criterion says that our minimum sampling frequency f_N should satisfy the following relation:

$$f_N \geq 2 \times 2\overline{f_x} \leftrightarrow \left(\frac{1}{p_\alpha}, \frac{1}{p_\beta}\right) \geq 4\overline{f_x} \leftrightarrow \overline{f_x} \leq \left(\frac{1}{4p_\alpha}, \frac{1}{4p_\beta}\right) \tag{13}$$

which means that for pixels of size (p_α, p_β), any frequency larger than $(1/4p_\alpha, 1/4p_\beta)$ would experience aliasing. Hence, to capture a frequency $\overline{f_x}$, the pixel size needs to be smaller than $1/4\overline{f_x}$ which for very high frequencies, is extremely small, causing the cost of the image sensor to be very high.

Aliasing, in general, distorts the signal in complex ways. For sinusoidal signals, however, aliasing produces a sinusoid of a different frequency. If one is capturing increasingly high frequency sinusoids with a lens-based system, aliasing will make the same frequencies appear more than once. We call this phenomenon frequency ambiguity. The next section discusses this phenomenon.

Optics EXPRESS

2.4. Frequency ambiguity in lens-based systems

One of the consequences of aliasing is that high frequencies appear similar to low frequencies. In this paper, we call this behavior ambiguity in frequency. Figure 3 shows this behavior in the context of a lens-based system. This is the form of signal corruption that Nyquist criterion aims to avoid.

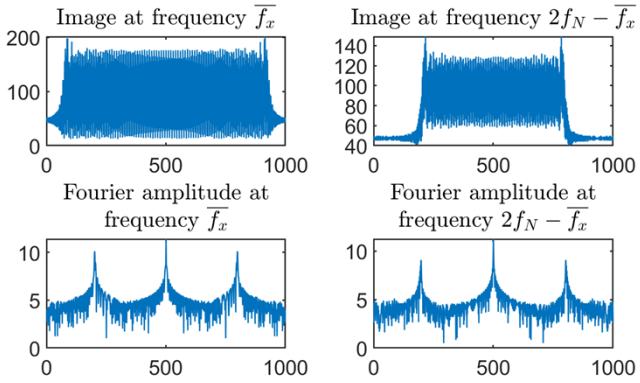

Fig. 3. Image and Fourier amplitude spectrum of two frequencies separated by the Nyquist frequency for a lens-based system. Here, f_N denotes the corresponding Nyquist frequency, and $\overline{f_x}$ is the input sinusoid frequency.

For a diffuser with low scattering angle (e.g. 0.25°), similar frequency ambiguity, as mentioned above, can be seen (see Fig. 4) to some extent. However, for a diffuser with high scattering angle (e.g. 15°), Fourier amplitude spectrum of the intensity patterns do not admit such visually identifiable ambiguities (see Fig. 5).

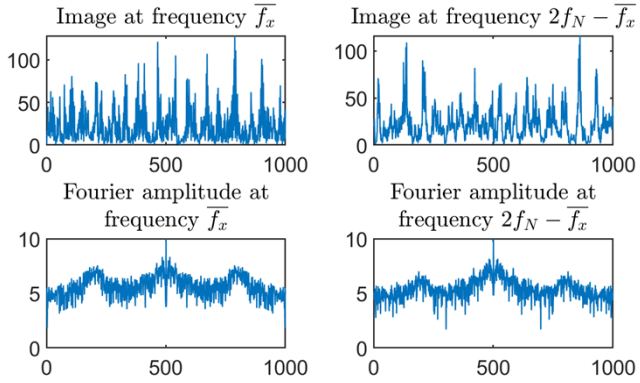

Fig. 4. Image and Fourier amplitude spectrum of two frequencies separated by the Nyquist frequency for a lensless SRPE system with 0.5° scattering diffuser. Here, f_N denotes the corresponding Nyquist frequency, and $\overline{f_x}$ is the input sinusoid frequency.

Hence, to investigate frequency ambiguities in lensless systems with high scattering diffusers, we employ a statistical measure of similarity, namely, normalized mutual information.

In order to probe the frequency ambiguity of a diffuser-based lensless SRPE system, we start with an SRPE system equipped with a diffuser with a specified scattering angle, and an image sensor with specified pixel size which defines the Nyquist frequency limit f_N of the input as well. Then we gradually increase the frequency of the input $\overline{f_x}$ (see Eq. (1)) from 0 to $4f_N$. For each such frequency $\overline{f_x}$, we obtain the intensity signature $u_2(\alpha, \beta; \overline{f_x})$ by using Eq. (1)–(8) and compute

Optics EXPRESS

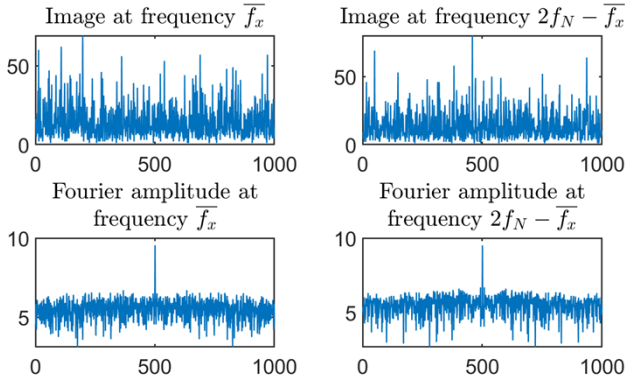

Fig. 5. Image and Fourier amplitude spectrum of two frequencies separated by the Nyquist frequency for a lensless SRPE system with 15° scattering diffuser. Here, f_N denotes the corresponding Nyquist frequency, and $\overline{f_x}$ is the input sinusoid frequency.

their Fourier spectrum $U_2(f_\alpha, f_\beta; \overline{f_x})$:

$$U_2(f_\alpha, f_\beta; \overline{f_x}) = \mathcal{F}[u_2(\alpha, \beta; \overline{f_x})] = A(f_\alpha, f_\beta; \overline{f_x}) \exp(j\phi(f_\alpha, f_\beta; \overline{f_x})) \tag{14}$$

where $\mathcal{F}[\cdot]$ denotes Fourier transform, (f_α, f_β) denotes the spatial frequencies corresponding to (α, β), $A(\cdot)$ denotes the amplitude spectrum, and $\phi(\cdot)$ denotes phase spectrum of $u_2(\cdot)$. Afterwards, we compute an amplitude gram matrix G_A and phase gram matrix G_ϕ such that its i-th row and j-th column satisfies the following relations:

$$G_A(i,j) = NMI(A(f_\alpha, f_\beta; \overline{f_x}[i]), A(f_\alpha, f_\beta; \overline{f_x}[j])) \tag{15}$$

$$G_\phi(i,j) = NMI(\phi(f_\alpha, f_\beta; \overline{f_x}[i]), \phi(f_\alpha, f_\beta; \overline{f_x}[j])) \tag{16}$$

where $\overline{f_x}[i]$ denotes the i-th input frequency, and $NMI(\cdot, \cdot)$ stands for the normalized mutual information between the input sequences (see Section 2.6). Both G_A and G_ϕ are symmetric matrices and their entries are bounded within the range $[0, 1]$ with diagonal entries equal to 1. If any off-diagonal entry $G_A(i,j)$ and/or $G_\phi(i,j)$ appears to be close to 1 or significantly higher than its neighboring region, we say that there is an ambiguity between frequencies $\overline{f_x}[i]$ and $\overline{f_x}[j]$, i.e., one of these frequencies can be mistaken as another.

Frequency ambiguity due to aliasing is a form of signal corruption that motivates Nyquist sampling criterion. Figure 5 and the discussion in Section 3.1 show us that such frequency ambiguities are absent in the case of lensless SRPE systems. Hence, we need to refer to the wave propagation in the SRPE systems to analyze how input frequencies are getting distributed on the image sensor, find limiting pixel sizes such that the signal variations are accurately captured, and reason about a plausible signal corruption that might occur when pixels are larger than their limiting size.

2.5. *Proposed sampling criterion for diffuser-based lensless SRPE systems*

In this paper, we aim to answer the following question: if a signal has maximum frequency f_m, what should be the largest pixel size (p_α, p_β) such that the corresponding intensity pattern $i_S[m,n]$ is able to capture the variation in the input signal? Since lens-based imaging produces visually interpretable images, one can answer this question for such systems using the classical Nyquist frequency criterion. Lensless SRPE systems, on the other hand, capture pseudorandom intensity patterns with high frequency features. Applying Nyquist criterion naively would beget

Optics EXPRESS

pixel sizes which are smaller than the diffuser features. This contradicts the success of recent SRPE advances [5, 6] where standard image sensors were used to capture patterns corresponding to diffusers with extremely fine features for purposes of disease classification. Hence, we look at the wave propagation mechanism of SRPE systems to answer this question.

Suppose that a given signal has a maximum frequency f_m. This maximum frequency component appears as a pure sinusoid of frequency f_m with a certain amplitude and phase. For the ease of this analysis, we need to find the maximum interval over which the function can be assumed not to be distorted. Nyquist criterion helps us in this regard. Nyquist criterion tells us that if a sinusoid of frequency f_m is sampled at a frequency f_S that is at least $2f_m$, the original signal and the sampled signal contain the same information. Hence, we can rewrite Eq. (4-5) by substituting the field $u_1(\zeta, \eta)$ right before the diffuser with its Nyquist sampled counterpart:

$$u'_{1\mathrm{N}}(\zeta, \eta) = u_{1\mathrm{N}}(\zeta, \eta) \times t_D(\zeta, \eta) \tag{17}$$

and,

$$u_{2\mathrm{N}}(\alpha, \beta) = u'_{1\mathrm{N}}(\alpha, \beta) * h_S(\alpha, \beta) * \frac{1}{2\pi} \frac{z_2}{r_2} \left(\frac{1}{r_2} - jk \right) \frac{\exp(jkr_2)}{r_2} \tag{18}$$

where $u_{1N}(\zeta, \eta)$ is derived from $u_1(\zeta, \eta)$ in the following way:

$$u_{1N}(\zeta, \eta) = \left(\sum_{m,n=-\infty}^{m,n=\infty} u_1(\zeta, \eta) \delta \left(\zeta - \frac{m}{f_S}, \eta - \frac{n}{f_S} \right) \right) * Rect \left(\frac{f_s}{2} \zeta, \frac{f_S}{2} \eta \right) \tag{19}$$

and $u_{2N}(\alpha, \beta)$ is the corresponding field that is incident on the image sensor. Note that, using a rectangular filter $Rect(\cdot, \cdot)$ instead of a Sinc filter of the same cut-off frequency will only scale the frequency spectrum of the cosine input without changing its overall profile (Fig. 6). The convolution operation in Eq. (19) merely employs a sample and hold operation, maintaining the sampled output at a constant level until the next sample appears. Figure 6 shows the effect of this sample and hold mechanism on a sinusoid. Please note that we are not attempting to sample the object field here. We merely want to be able to maintain the object field at a constant level over a maximum interval without harming its frequency spectrum. Sample and hold at the corresponding Nyquist frequency merely gives us a principled way to achieve this.

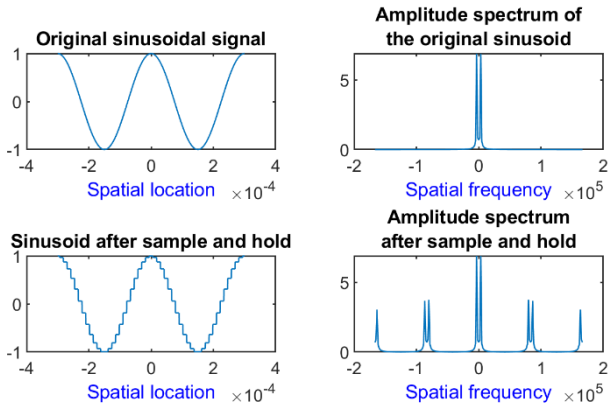

Fig. 6. Spatial and amplitude spectrum plot of a sinusoid before and after the operation of a sample and hold mechanism. The repetition of frequency content in the amplitude spectrum after sample and hold is due to the sampling operation. The phase spectrum is zero due to both signals being even.

Interestingly, Fig. 6 shows that the frequency spectrum of a sinusoid after sample and hold operation includes a number of replicas of the original frequency spectrum. They appear due to

Optics EXPRESS

the sampling operation. It is reasonable to suspect at this point that these high frequency replicas might interfere with this study. However, keep in mind that when we perform this analysis, we are only concerned with the highest frequency content f_m of a provided input signal, as mentioned in the beginning of this section. Hence, any frequency higher than this, as long as they are well separated and do not modify the main frequency component (central part of the spectrum) via aliasing, are harmless to this analysis.

Since we are interested in finding the limiting pixel size, we obtain $u_{1N}(\cdot,\cdot)$ from the perfect sinusoid $u_1(\cdot,\cdot)$ using its Nyquist sampling frequency, i.e., $f_S = 2f_m$ [see Eqs. (17)–(19)]. Under this condition, the $u_{1N}(\cdot,\cdot)$ would produce two distinct values during each spatial period and all the other values would be exact replicas of these two values. These two values get modulated by the diffuser transmittance function $t_D(\zeta,\eta)$ and show up at the image sensor. Figure 7 shows this process visually. In Fig. 7, we call these two distinct values samples of $u_{1N}(\zeta,\eta)$ for convenience.

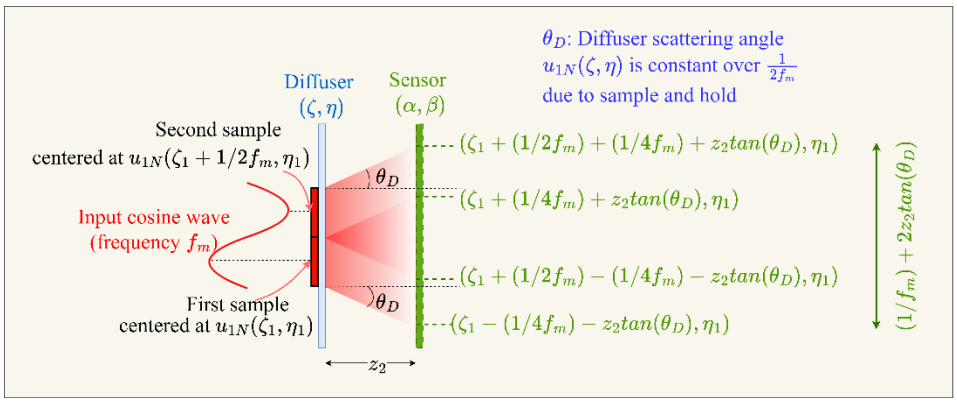

Fig. 7. The scattering of the diffuser when a sinusoidal wave sampled and reconstructed at Nyquist frequency using sample and hold operation is incident on a diffuser. Since we get two distinct samples per period of a sinusoid at Nyquist sampling, we isolate two neighboring samples and observe their effects on the sensor plane.

Say, a sinusoid $u_{1N}(\zeta,\eta)$ has appeared just before the diffuser. We have two distinct samples per spatial period of $u_1(\zeta,\eta)$, i.e. $1/f_m$. We suppose that these two samples appear at co-ordinates (ζ_1,η_1) and $(\zeta_1 + 1/2f_m, \eta_1)$ (see Fig. 7). Now, we assume that the diffuser surface features have frequencies higher than the frequency of the input sinusoid. This assumption comes from the literature of Direct Sequence Spread Spectrum communication [13] where the modulating signal needs to be of a frequency higher than that of the input signal. Under this assumption, the diffuser features are of similar size or smaller than $1/f_m$, causing the input signal to be constant over multiple diffuser features.

When the above assumption is satisfied, the diffuser will spread their corresponding fields over a certain area of the image sensor. The input at (ζ_1,η_1) will be spread between $(\zeta_1 - (1/4f_m) - z_2\tan(\theta_D), \eta_1)$ and $(\zeta_1 + (1/4f_m) + z_2\tan(\theta_D), \eta_1)$ (see Fig. 7). The input at $(\zeta_1 + 1/2f_m, \eta_1)$ will be spread between $(\zeta_1 + (1/2f_m) - (1/4f_m) - z_2\tan(\theta_D), \eta_1)$ and $(\zeta_1 + (1/2f_m) + (1/4f_m) + z_2\tan(\theta_D), \eta_1)$ (see Fig. 7). When we sample this field at the sensor, we need to collect information from both samples of $u_{1N}(\zeta,\eta)$ at (ζ_1,η_1) and $(\zeta_1 + 1/2f_m, \eta_1)$. In order to derive the largest sampling rate for the sensor, we look at where the terminal rays from these inputs are incident on the sensor. From Fig. 7, we see that the distance between these terminal rays is $(1/f_m) + 2z_2\tan(\theta_D)$. If the pixel size is any larger than this, the two inputs get absorbed within the same pixel, reducing the variability of the captured signal. Hence, meaningful complex field variations happen on the sensor plane at a frequency of $((1/f_m) + 2z_2\tan(\theta_D))^{-1}$. The field,

Optics EXPRESS

however, contains much finer variations due to fine diffuser features, but such variations do not contain anything meaningful about the original signal.

The above discussion shows that variation in the sinusoidal field behind the diffuser is rendered at a frequency $((1/f_m) + 2z_2 \tan(\theta_D))^{-1}$ on the sensor plane. Since the sensor captures the intensity of this field, and since intensity is correlation in the frequency domain, the same information is rendered at a frequency $2 \times ((1/f_m) + 2z_2 \tan(\theta_D))^{-1}$. To decide an optimal sampling rate for the image sensor, we need to ensure this information is optimally captured. Nyquist criterion tells us that the minimum sampling frequency f_{Sdiff} would now be twice of this frequency, i.e.,

$$f_{Sdiff} = 4 \times \left(\frac{1}{f_m} + 2z_2 \tan(\theta_D) \right)^{-1} \tag{20}$$

which causes the maximum pixel size $p_{Maxdiff}$ to be the following:

$$p_{Maxdiff} = \frac{1}{f_{Sdiff}} = \frac{1}{4f_m} + \frac{z_2 \tan(\theta_D)}{2} \tag{21}$$

When the pixels are made larger, both parts of the input get absorbed within the same pixel. From the point-of-view of the pixels, it is as though the input signal has no variation. Hence, from this point onwards, the output of the pixels begins to look as though the input has 0 frequency. This means that, for a particular pixel size, if we increase the input frequency from 0, the similarity between intensity pattern at input frequency and intensity pattern at 0 frequency will gradually decrease. When the frequency crosses the sampling frequency limit for that pixel size, this similarity should then start to increase. Section 3.2 verifies this hypothesis using numerical simulations and by using normalized mutual information (NMI) as the similarity metric.

We note that, when a lens with focal length f_l is used to image an object such that $z_1 = z_2 = 2f_l$, the sensor field and the object field become almost identical, i.e., there is no spreading/redistributing of object information on the image plane. For these scenarios, since there is no scattering from the lens, i.e., $\theta_D = 0$, the maximum pixel size $P_{Maxlens}$ becomes:

$$P_{Maxlens} = \frac{1}{4f_m} + z_2 \tan(0) = \frac{1}{4f_m} \tag{22}$$

which is the same as what was derived in Section 2.3 using the Nyquist criterion. Our method generalizes this criterion for diffuser-based lensless SRPE systems. It is also worthwhile to note that since lenses do not scatter light and have transmittance functions which are fundamentally different from those of diffusers, the observation of Eq. (22) cannot be extended to situations where $z_1 \neq z_2$. In such cases, the optimal pixel size for lens-based system becomes $|M|/4f$ where $M = -z_2/z_1$ is the magnification of the lens-based system.

A quick look at Eq. (21) suggests that the optimal pixel size might increase indefinitely with z_2. It is important to remember that the intensity pattern captured at the sensor becomes of lower light level as z_2 increases. After a certain z_2, the intensity pattern gets overcome by noise, leading to a very low signal to noise ratio (SNR). Hence, the optimal pixel size for these scenarios becomes limited by the SNR. Also, as the pixel size increases, collection of a reasonable number of pixels requires the image sensor to be to be very large, making such pixel sizes to be infeasible. Hence, while putting Eq. (21) to use, one must keep in mind the feasibility of the maximum pixel size.

2.6. Mutual information

Mutual information (MI) $I(X;Y)$ [14] is a statistical measure of dependence between two random variables X and Y. If X and Y are stationary continuous random variables with joint probability density function (PDF) $f_{X,Y}(x,y)$ and marginal PDFs $f_X(x)$ and $f_Y(y)$ respectively, the MI can be

Optics EXPRESS

given as below:

$$I(X;Y) = \iint f_{X,Y}(x,y) \log\left(\frac{f_{X,Y}(x,y)}{f_X(x) f_Y(y)}\right) dxdy \tag{23}$$

Unlike correlation that measures linear dependence between X and Y, $I(X;Y)$ is able to capture non-linear dependencies between random variables as well. It measures how much entropy of X is explained by Y. In other words, given knowledge of Y, it shows how much uncertainty remains in the estimation of X i.e.,

$$I(X;Y) = H(X) - H(X|Y) \tag{24}$$

where $H(X)$ is the entropy of X and $H(X|Y)$ is the entropy of X given Y.

Note that $I(X;Y)$ is 0 if and only if X and Y are statistically independent and it increases as they become more dependent. It can also be intuitively interpreted as the Kullback-Leibler divergence between the joint PDF of (X, Y) and the product of their marginal PDFs. MI also has the attractive property that it is invariant under homeomorphic transformations (e.g. translation, rotation, scaling etc.) of the underlying random variables.

However, MI is not a normalized measure. That is, with increasing dependency between X and Y, MI increases without an upper bound. Normalization is important since we are using it to perform a comparative study. Hence, we obtain a normalized metric using the following equation:

$$\overline{I(X;Y)} = \frac{I(X;Y)}{\sqrt{H(X)H(Y)}} \tag{25}$$

where $H(X)$ and $H(Y)$ are the entropies of X and Y respectively. For all our analyses, we have assumed that the 1-dimensional (1D) histogram of a pattern X sufficiently approximates the PDF of X.

3. Results

We use angular spectrum propagation to mathematically simulate an SRPE system. This is an ideal choice because for some of the simulations, the propagation distances z_1, z_2 and the diffuser scattering angle θ_D make the paraxial approximation invalid, precluding the use of Fresnel diffraction model. The parameters common for all simulations have been reported in Table 1. For both simulations performed in this study, we needed to gradually vary the input frequency within an extremely large range. This is difficult to perform in a real-world experiment. Since angular spectrum propagation is highly accurate, and the thin diffuser model can be easily parameterized to mimic diffusers with different scattering angles [8], the simulation results can be safely assumed to be close to reality given the lateral sampling rates for the object plane, diffuser plane and the image sensor plane have been judiciously chosen. Keeping in mind that for a light of wavelength λ, the angular spectrum propagation kernel has a cut-off frequency $1/\lambda$, the lateral sampling rate of the object plane, diffuser plane, and the sensor plane have been maintained at half the wavelength to avoid aliasing during simulation. This, however, causes us to sample 94491 different locations on each of the planes. To keep the computation burden within reasonable limits, we have performed our simulations on one dimension (1D). Note that the aperture sizes for both the diffuser and the lens have been kept at 3 centimeters to avoid high computational burden. Although this aperture seems small, care has been taken to ensure that the input frequencies for all simulations are always below the limit dictated by the numerical aperture of lenses/diffusers. We have exercised this caution to ensure high accuracy of the simulation results. For real-world experiments where optical wave propagations and interaction between wave and optical elements happen naturally, such concerns are absent and hence do not hinder the applicability of this theory.

Optics EXPRESS

Table 1. Simulation parameters used in this study (m denotes meters). These parameters are common to both lensless and lens-based systems.

Parameters	Values	Parameters	Values
Wavelength of light λ	6×10^{-7} m	Lateral sampling rate τ	3×10^{-7} m
Diffuser/Lens aperture size	3×10^{-2} m	Sensor dimension (size)	3×10^{-2} m

3.1. *Frequency ambiguity in lensless and lens-based systems*

As discussed in Section 2.4, we compute the amplitude gram matrix G_A and the phase gram matrix G_ϕ for a lensless system (Fig. 8) and a lens-based system (Fig. 9). Note that in Figs. 8 and 9, the horizontal and the vertical axes have the same label. This is because the x-axis and the y-axis in Figs. 8 and 9 denote the columns and the rows of the corresponding gram matrices. In Eqs. (15 and 16), we see that both the rows and columns of gram matrices are being indexed by the same quantity namely, the input frequencies. The diagonal locations in Figs. 8 and 9 show the NMI between intensity patterns of the same input frequencies and the off-diagonal locations show NMI between patterns of dissimilar frequencies. Whenever there is a predictable pattern of unusually high values at the off-diagonal locations, we can tell that there is a frequency ambiguity, i.e., one input frequency can be misread as another. The goal of this study was to verify whether there is an identifiable pattern of frequency ambiguity for lensless SRPE systems. If there is such a pattern, it can be utilized to define a lower limit of sampling frequency (conversely, an upper limit for the pixel size) for such systems. The parameters for this simulation are given in Table 2 below. The parameter values have been chosen to mimic real-world experiments. Note that the object to lens distance and the lens to sensor distance have been kept equal. This has been done to avoid any frequency scaling due to magnification by lenses. Similar distances have been used for diffusers to provide a fair comparison. Also note that the propagation distances listed in Table 2 are small. This is not due to any physical limitation of the optical devices under study. Once we choose a practical sensor pixel size, the maximum permissible frequency for the input signal (referred to as Nyquist frequency) is decided. The studies in this section require that the numerical aperture of the lens/diffuser be high enough such that input frequencies which are many times higher than the Nyquist frequency can be captured by the lens/diffuser. Since we have already kept the aperture size of the lens/diffuser small to ease the computational burden for the simulations, we had to keep the object to lens/diffuser distances small to satisfy the above requirement. Using a more realistic distance would increase the computational burden for simulation but would not change the conclusions of this study.

Table 2. Simulation parameters for studying frequency ambiguity (m denotes meters).

Parameters	Values	Parameters	Values
Object to lens distance	6×10^{-2} m	Object to diffuser distance	6×10^{-2} m
Lens to sensor distance	6×10^{-2} m	Diffuser to sensor distance	6×10^{-2} m
Focal length of the lens	3×10^{-2} m	Image sensor pixel size	3.6×10^{-6} m
Aperture size of lens	3×10^{-2} m	Number of camera pixels	2001

As seen in Fig. 8, the amplitude gram matrix G_A and the phase gram matrix G_ϕ for lensless systems admit no such identifiable frequency ambiguity even when the input frequency has been increased to 4 times the Nyquist frequency for the corresponding pixel size. There are some sporadic high values on the off-diagonal places in G_A due to the statistical nature of the spatial variations in the intensity patterns but nothing is even close to the diagonal values which denote the self-similarities at individual frequencies. A careful observation of the amplitude gram matrix G_A for lensless systems in Fig. 8 shows that frequencies higher than 3 times the

Optics EXPRESS

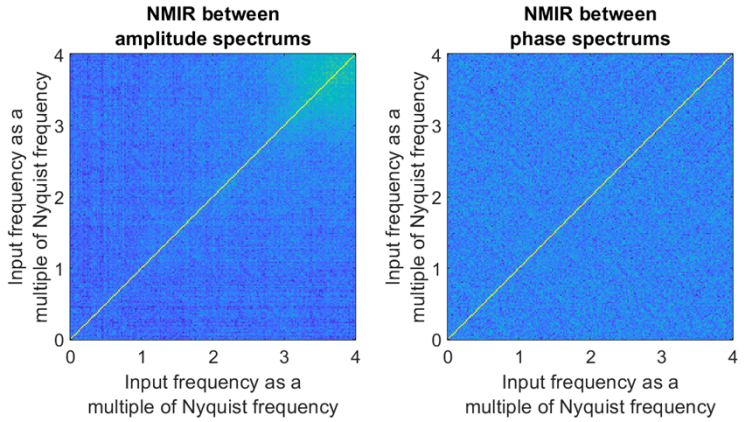

Fig. 8. Visualization of the amplitude gram matrix G_A (left) and the phase gram matrix G_ϕ (right) for lensless SRPE systems. Yellow denotes a high similarity (close to 1) and blue denotes a low similarity (close to 0).

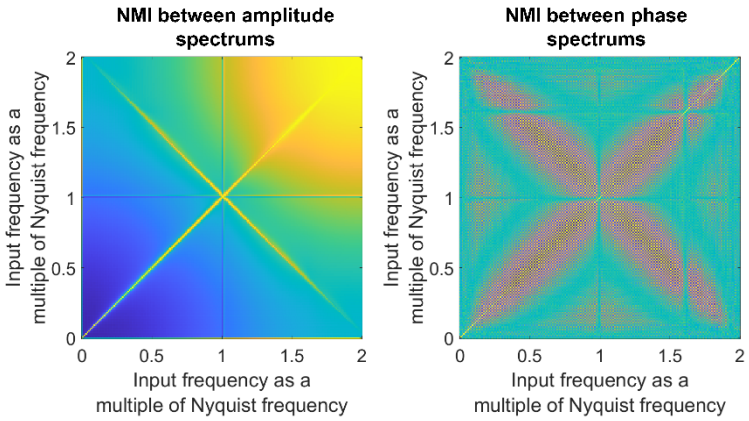

Fig. 9. Visualization of the amplitude gram matrix G_A and the phase gram matrix G_ϕ for lens-based systems. The extra diagonal line going from top-left to bottom-right of the amplitude and phase gram matrices denote frequency ambiguity due to aliasing.

Nyquist frequency exhibit a higher similarity amongst themselves. This is because in such cases, the input frequencies are extremely close to the numerical aperture limit of the diffuser. The input light has been diffracted so far off the optical axis that the spatial variations in the output intensity pattern have become of much lower light level, making it difficult to render for an 8 bit image sensor. A 10 or 12-bit image sensor has better dynamic range, i.e., they can capture finer changes in the intensity levels. This means that the off-diagonal regions in the top right part of the amplitude Gram Matrix G_A (as shown in Fig. 8 [left]) would have shown values much lower than it is currently showing. As our objective is to show the absence of frequency ambiguity in lensless systems (the diagonal region should have values significantly higher than the off-diagonal regions), opting for a 10 or 12-bit image sensor would have been beneficial for our study. However, as 8-bit sensors are the ones most commonly used for practical experiments and since it demonstrates the absence of frequency ambiguity reasonably well, we have chosen an 8-bit sensor for this study.

When we perform the same analysis on lens-based systems with a perfect lens, we observe the classic phenomenon of aliasing. The amplitude gram matrix G_A (left plot in Fig. 9) shows

Optics EXPRESS

that when the input frequency goes above the Nyquist frequency corresponding to the pixel size of the image sensor, the resulting intensity pattern exhibits a high similarity with the intensity pattern of a lower frequency. Specifically, when the input frequency $\overline{f_x}$ is higher than the Nyquist frequency f_N, it produces a pattern that looks similar to the intensity pattern corresponding to the input frequency $(2f_N - \overline{f_x})$.

The above results show that looking for frequency ambiguity or aliasing might not be a valid sampling strategy for lensless systems. Due to the high frequency diffuser surface features, lensless SRPE systems continue to produce unique patterns even when the input frequency has increased far beyond the Nyquist frequency for the given pixel size. Hence, we need to look for a different kind of signal corruption. Section 2.5 gives us a possible signal corruption in diffuser intensity patterns. The next section verifies whether such signal corruptions actually manifest.

3.2. Assessing sampling criterion with normalized mutual information

In this section, we attempt to verify our proposed sampling criterion by applying statistical tools on a mathematically simulated SRPE system. The distance z_2 between the diffuser and the image sensor is usually very large (of the order of a few centimeters) compared to the pixel size of a typical camera (in microns). Also, in typical SRPE setups (e.g. [5,6]), the diffusers used have very high scattering angle (40°). Applying Eq. (21), we see that for such cases, the maximum permissible pixel size $P_{MaxDiff}$ assumes a very high value. Hence, we need to keep z_2 and θ_D sufficiently small so the limiting pixel size is small enough. This will allow an image sensor of practical size to contain a reasonable number of pixels in the limiting scenario. Using a smaller θ_D also forces us to choose a smaller input frequency $\overline{f_x}$ since the diffuser features need to be of higher frequency than the input signal. Keeping all these constraints in mind, we maintain the z_2 at 0.5 centimeters. We sample 4 different scattering angle values, i.e. [5°, 10°, 15°, 20°], for θ_D. For each θ_D, we decide a critical frequency $\overline{f_c}$ equal to $0.3f_D$ where f_D is the diffuser surface feature frequency (dependent on θ_D). According to this frequency, we calculate the maximum pixel size according to Eq. (21). For diffusers of scattering angle [5°, 10°, 15°, 20°], the maximum pixel sizes are $[225\mu m,\ 443\mu m, 671\mu m, 911\mu m]$ and the number of pixels are $[133, 67, 45, 33]$. Afterwards, we sample 1000 input frequencies in the range $[0, 2\overline{f_c}]$. For each such input frequency $\overline{f_x}$, we compute Eq. (1)–(8) to compute their corresponding intensity pattern $i_\Sigma(\overline{f_x})$. Then, we compare each such pattern with the intensity pattern at 0 input frequency $i_\Sigma(0)$ (i.e. spatially uniform input). We use normalized mutual information (NMI) by computing Eq. (23-25) for this comparison.

If our theory (as given in Section 2.5) is correct, $NMI(i_\Sigma(\overline{f_x}), i_\Sigma(0))$ should decrease from 1 as $\overline{f_x}$ increases from 0, attain its lowest value at $\overline{f_x} = \overline{f_c}$ and begin to increase again. This is due (also discussed in Section 2.5) to the fact that for the decided pixel size, if the input frequency goes beyond $\overline{f_c}$, one entire cycle of the input sinusoid gets absorbed by a single pixel. Since the sinusoid is repeating every cycle, from the viewpoint of the sensor pixels, the input signal begins to appear as though it is spatially uniform. In Fig. 10(a-d), we observe exactly this behavior. These plots have been obtained with different values of the diffuser scattering angle θ_D. The vertical dashed line in all the plots denote the theoretical limiting frequency ($\overline{f_c}$ for this discussion) at which the chosen pixel size begins to render erroneous sampling. Hence, for the input frequency $\overline{f_c}$, the chosen pixel size becomes the limiting pixel size. The fact that the simulationally obtained minima of all these plots coincide with $\overline{f_c}$ corroborates our proposed theoretical analysis.

It is reasonable to ask at this point why the minimum NMI in all the plots in Fig. 10 have values greater than zero. This is because even though the input signals are different, the diffuser used for obtaining both patterns on which the NMIs are calculated is the same. Since the diffuser surface roughness contributes heavily to the contrast in the intensity patterns, the presence of the same diffuser for both patterns causes the mutual information to remain at a significant level even when the frequencies are changing.

Optics EXPRESS

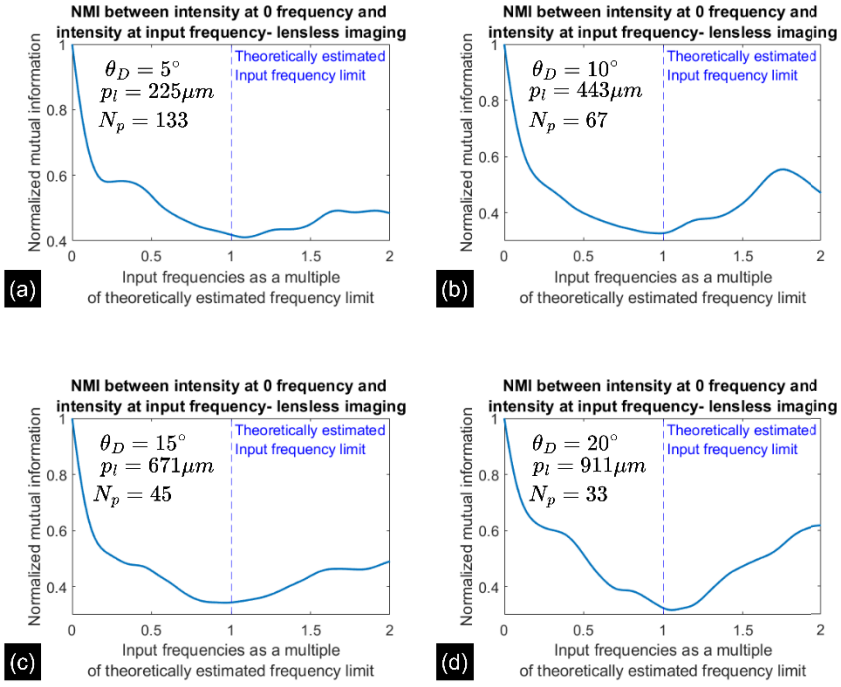

Fig. 10. Lensless SRPE normalized mutual information (NMI) [see Eq. (23)–(25)] of captured image sensor intensity patterns between intensity at 0 frequency and intensity at various input frequencies for diffusers with different scattering angles. The minima of these plots denote the frequency at which the chosen pixel sizes become the limiting pixel sizes. The theoretically obtained estimate of this frequency (dashed line) coincides with the simulation estimate. θ_D is the scattering angle of diffusers, p_l is the maximum pixel size and N_p is the number of image sensor pixels.

Note that, for calculating the maximum pixel size corresponding to an input frequency for a lens-based system, we can use the Nyquist criterion as discussed in Section 2.3. For a lens of focal length f_l, if the propagation distances are maintained such that $z_1 = z_2 = 2f_l$, proper sampling of the intensity pattern for an input frequency $\overline{f_x}$ would require the maximum pixel size for an image sensor to be $1/(4\overline{f_x})$ (independent of focal length) [see Eq. (22)]. However, the maximum pixel size for a lensless SRPE system for the same input and a diffuser with scattering angle θ_D would be $1/(4\overline{f_x}) + z_2\tan(\theta_D)/2$ [see Eq. (21)]. As $\overline{f_x}$ increase, the maximum pixel size decreases quickly to approximately 0 for lens-based systems and approximately $(z_2\tan(\theta_D)/2)$ for lensless systems. This is the behavior we see in Fig. 11(a). For a fixed frequency, the maximum pixel size increases with the scattering angle of the diffuser. This happens because as the diffuser scattering angle becomes higher, information about finer details in the input signal gets spread out over a larger area of the sensor. The ratio of the maximum pixel size of a lensless SRPE system to a lens-based system would be:

$$\frac{\text{max pixel size of lensless system}}{\text{max pixel size of lens} - \text{based systems}} = \frac{1/(4\overline{f_x}) + z_2\tan(\theta_D)/2}{1/(4\overline{f_x})} = 1 + 2\overline{f_x}z_2\tan(\theta_D) \quad (26)$$

For a fixed z_2 (the value of z_2 used for this study has been mentioned previously in this section), this ratio increases with $\overline{f_x}$. This is because as the input frequency increases, the Nyquist

Optics EXPRESS

criterion-dictated maximum pixel size of the lens-based system keeps reducing but the maximum pixel size of lensless SRPE systems converges to $(z_2 \tan(\theta_D)/2)$ which is significantly larger than 0 for all θ_D considered in this study. Figure 11(b) shows the ratio derived in Eq. (26). We observe that for the chosen z_2, the ratio reaches above 100 for high frequencies. This shows that lensless SRPE systems are especially beneficial for higher frequencies. Also, using lensless SRPE systems, we can use pixel sizes which are orders of magnitude larger than those required for lens-based systems.

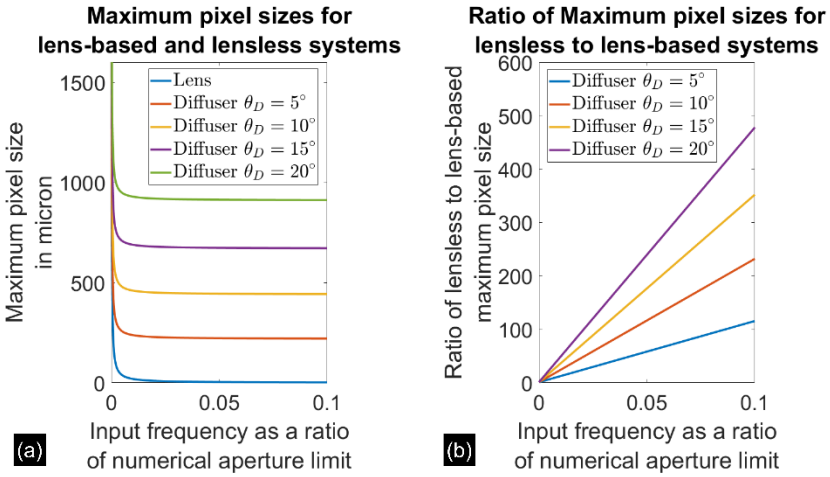

Fig. 11. Comparison of maximum image sensor pixel-size requirements between lens-based and lensless SRPE systems. Figure (a) shows the corresponding maximum pixel values. Figure (b) shows the ratio between the maximum pixel sizes of lensless SRPE systems to lens-based systems. The numerical aperture of the diffusers and the lens have been kept equal.

In closing, we would like to note that although this study has been based on well-established theories and mathematical models, an experimental confirmation would add immense practical value to these findings. In order to achieve this, we shall have to observe the output of SRPE systems for single frequency 1D input sinusoidal patterns. However, to get experimental results corresponding to Fig. 10, we need an experimental method to vary the input frequency over a large range. We are currently exploring some potential approaches to achieve this. Future developments on this work shall include experimental confirmations of this study.

4. Conclusion

In conclusion, we have formulated a principle to estimate the sampling criterion for lensless SRPE systems. Since lensless systems do not exhibit frequency ambiguities due to aliasing like their lens-based counterparts, we have looked at the wave propagation through the system to investigate what kind of signal corruption might occur when sampling goes awry. We have proposed a pixel size limit for a given input signal frequency for lensless SRPE systems. We then performed numerical simulations using angular spectrum propagation and mutual information to verify that the anticipated data corruption was indeed happening, and it was happening at the proposed sampling limit. When the input signal has frequencies lower than the frequency of the diffuser surface features, the limiting pixel size for lensless SRPE systems increases with scattering angle of the diffuser. It also increases with diffuser to sensor distance with a caveat that the captured intensity also becomes dimmer, reducing the SNR. This work provides a principled way to optimize SRPE systems in scenarios where acquisition of high frequency

Optics EXPRESS

information is of critical importance. For such scenarios, using lensless SRPE systems rather than lens-based systems allows us to accomplish imaging/sensing using cameras with much bigger pixels which may be critical in exotic image sensors such as infrared imaging [15]. In future, we shall investigate how the findings of this study change if the pseudorandom diffuser is replaced with a diffraction grating with specified surface structures. As regular surfaces are characterized by their own parameters, it might be possible to factor such parameters in this study. Future works will also consider other statistical approaches [16–18] and various applications [19–22] and the experimental confirmation of this study.

Funding. Air Force Research Laboratory (FA8650-21-C-5711); Air Force Office of Scientific Research (FA9550-21-1-0333, FA9550-24-1-0128); Office of Naval Research (N000142212375, N000142212349); National Science Foundation (# 2141473).

Acknowledgements. We gratefully acknowledge the Air Force Research Laboratory, Materials and Manufacturing Directorate (AFRL/RXMS) for the support and valuable discussions via Contract No. FA8650-21-C-5711. B. Javidi acknowledges support under The Office of Naval Research (ONR) (N000142212375; N000142212349); Air-Force Office of Scientific Research (AFOSR) (FA9550-21-1-0333; FA9550-24-1-0128), and National Science Foundation grant # 2141473. The authors are also grateful to Kashif Usmani for the valuable discussions and comments on the manuscript. Any opinions, findings, and conclusions or recommendations expressed in this paper are those of the authors and do not necessarily reflect the views of the United States Department of Defense.

Disclosures. The authors declare no conflicts of interest.

Data availability. No data were generated or analyzed in the presented research.

References

1. J. W. Goodman, *Introduction to Fourier optics*, 3rd ed. (Roberts and Company Publishers, 2005).
2. A. Stern and B. Javidi, "Random projections imaging with extended space-bandwidth product," J. Display Technol. **3**(3), 315–320 (2007).
3. B. Javidi, A. Markman, and S. Rawat, "Automatic multicell identification using a compact lensless single and double random phase encoding system," Appl. Opt. **57**(7), B190–B196 (2018).
4. B. Javidi, S. Rawat, S. Komatsu, *et al.*, "Cell identification using single beam lensless imaging with pseudo-random phase encoding," Opt. Lett. **41**(15), 3663–3666 (2016).
5. T. O'Connor, C. Hawxhurst, L. M. Shor, *et al.*, "Red blood cell classification in lensless single random phase encoding using convolutional neural networks," Opt. Express **28**(22), 33504–33515 (2020).
6. P. M. Douglass, T. O'Connor, and B. Javidi, "Automated sickle cell disease identification in human red blood cells using a lensless single random phase encoding biosensor and convolutional neural networks," Opt. Express **30**(20), 35965–35977 (2022).
7. S. Goswami, P. Wani, G. Gupta, *et al.*, "Assessment of lateral resolution of single random phase encoded lensless imaging systems," Opt. Express **31**(7), 11213–11226 (2023).
8. S. Goswami, G. Krishnan, and B. Javidi, "Robustness of single random phase encoding lensless imaging with camera noise," Opt. Express **32**(4), 4916–4930 (2024).
9. N. Antipa, G. Kuo, R. Heckel, *et al.*, "DiffuserCam: lensless single-exposure 3D imaging," Optica **5**(1), 1–9 (2018).
10. R. Corman, W. Boutu, A. Campalans, *et al.*, "Lensless microscopy platform for single cell and tissue visualization," Biomed. Opt. Express **11**(5), 2806–2817 (2020).
11. N. Antipa, P. Oare, E. Bostan, *et al.*, "Video from Stills: Lensless Imaging with Rolling Shutter," in *2019 IEEE International Conference on Computational Photography (ICCP)*, 1–8 (2019).
12. J. Goodman, *Speckle Phenomena in Optics: Theory and Applications*, 2nd ed. (SPIE Press, 2020).
13. P. Flikkema, "Spread-spectrum techniques for wireless communication," IEEE Signal Process. Mag. **14**(3), 26–36 (1997).
14. T. M. Cover and J. A. Thomas, *Elements of information theory*, 2nd Ed. (John Wiley & Sons, 1999).
15. G. Aschenbrenner, K. Usmani, S. Goswami, *et al.*, "Lensless object classification in long wave infrared using random phase encoding," Opt. Eng. **63**(11), 111809 (2024).
16. B. Moghaddam, C. Nastar, and A. Pentland, "A Bayesian similarity measure for direct image matching," *Proceedings - International Conference on Pattern Recognition 2*, 350–358 vol.2 (1996).
17. C. Liu, "The Bayes decision rule induced similarity measures," IEEE Trans. Pattern Anal. Machine Intell. **29**(6), 1086–1090 (2007).
18. A. Gretton, K. Fukumizu, C. H. Teo, *et al.*, "A kernel statistical test of independence," in *20th Advances in neural information processing systems* (2007).
19. Z. Stein and A. Stern, "Imperceptible CMOS camera dazzle for adversarial attacks on deep neural networks," arXiv (2023).

Optics EXPRESS

20. A. Stern and V. Kravets, "Compressive Learning Holography with LPTNet," *Optica Imaging Congress 2024 (3D, AOMS, COSI, ISA, pcAOP)* (2024), paper DW3 H.2 (2024).
21. V. Kravets, B. Javidi, and A. Stern, "Compressive imaging for thwarting adversarial attacks on 3D point cloud classifiers," Opt. Express **29**(26), 42726–42737 (2021).
22. V. Kravets, B. Javidi, and A. Stern, "Compressive imaging for defending deep neural networks from adversarial attacks," Opt. Lett. **46**(8), 1951–1954 (2021).